nature communications

Article https://doi.org/10.1038/s41467-026-70057-3

Spatio-spectral light-by-light moulding in multimode fibre

Received: 10 June 2025

Accepted: 10 February 2026

Published online: 07 March 2026

Check for updates

Yago Arosa[1,2,5], Tigran Mansuryan[1,5], Arnaud Poisson[1], Wasyhun Asefa Gemechu[3], Katarzyna Krupa[4], Mario Ferraro[3], Fabio Mangini[3], Benjamin Wetzel[1], Stefan Wabnitz[3], Alessandro Tonello[1] & Vincent Couderc[1] ✉

Controlling complex light waves to achieve desired behaviours or characteristics on demand presents a significant challenge. This task becomes even more complicated when manipulating speckled light beams, owing to their inherently fuzzy intensity and phase structures. Here we demonstrate that a weak speckled second-harmonic signal in a multimode graded-index fibre can be manipulated via its conservative interaction with a high-power co-propagating fundamental pump wave. Specifically, the spatial quality of the signal can be either enhanced or degraded by varying the pump's power or its modal distribution. The underlying physical mechanism is the optically induced mode conversion that can be controlled by the pump beam shape. This phenomenon enables new possibilities to manipulate complex light in nonlinear multimode waveguides. A striking example of this novel light-by-light control is the experimentally observed enhancement or partial suppression of the visible Raman Stokes cascade regulated by the second harmonic beam, while modulated by the mode power distribution of the fundamental beam.

The manipulation of light-by-light through cross-phase modulation (XPM) via the Kerr effect was extensively studied in the 1980s and 1990s[1–7]. The Kerr-induced cross-action of an intense pump light beam can alter a weak copropagating probe beam's temporal, spectral and spatial profiles. This interaction occurs conservatively without any power exchange between the pump and the probe. For instance, the additional phase shift that is induced by the strong wave may enable phase-matching between a fundamental frequency (FF) beam and its second harmonic (SH), allowing the control of nonlinear frequency conversion processes[2]. A lesser-known method for conservative control between light beams of different frequencies is the optically induced mode coupling (OIMC). This parametric interaction permits frequency translation without exponential gain, thereby avoiding spontaneous noise emission. As a result, the frequency translation associated with OIMC preserves the quantum state of a signal[8,9]. OIMC can involve two pumps at different wavelengths: maximum conversion efficiency from a signal to an idler is obtained at phase matching, under various configurations of polarisation states, spatial modes, and wavelengths for pumps, signals, and idlers[10–12].

Nonlinear effects in multimode optical fibres provide a leap in our capacity for all-optical light manipulation: recent experiments have revealed that controlling the input wavefront permits shaping the spatial, temporal, and spectral properties of highly multimode beams[13,14]. In this framework, the effect of Kerr beam self-cleaning (BSC)[15–26], which allows the transformation of a speckle into a quasi-single-mode beam at the output of a graded-index (GRIN) highly multimode optical fibre (MMF), is particularly intriguing. BSC was initially interpreted as a nonlinear interaction between linear beam self-imaging and Kerr nonlinearity. The resulting nonlinear refractive index long-period grating[15,16] facilitates the phase-matching of frequency degenerate inter-modal four-wave mixing (IM-FWM), thus enhancing the nonlinear power redistribution[16–18]. From the

[1]Université de Limoges, XLIM, UMR CNRS 7252, Limoges, France. [2]iMATUS, University of Santiago de Compostela, Praza do Obradoiro S/N, Santiago de Compostela, Coruña, Spain. [3]DIET, Sapienza University of Rome Via Eudossiana 18, Rome, Italy. [4]Institute of Physical Chemistry, Polish Academy of Sciences, Warsaw, Poland. [5]These authors contributed equally: Yago Arosa, Tigran Mansuryan. ✉e-mail: Vincent.couderc@xlim.fr

application point of view, the most important aspect of BSC is the enhancement of the beam spatial quality, that is, the quenching of the beam's M^2 factor. Although it is a purely conservative process, BSC has also been observed in lossy and gain fibres[24,25] and in active tapers[27,28]. This has opened a new avenue for developing powerful fibre lasers operating in Q-switched or mode-locked configurations[25,26,29–31]. Experiments have shown that BSC maintains the spatial coherence of the input laser[32], which enables new applications, such as imaging through MMFs[33]. Nevertheless, explaining the underlying mechanism for BSC has led to an ongoing controversial debate. Currently, the most widely accepted theory of BSC is based on thermodynamic considerations[34–36]. Within such a theoretical framework, the concept of BSC has been extended to the nonlinear dynamics of two co-propagating, orthogonally polarised beams[37–40]. However, experimental demonstrations of BSC involving multiple beams have so far been limited to a single strong carrier wavelength, thus preventing applications of this effect to polychromatic beams. Our approach opens new opportunities for supercontinuum generation in multimode fibres by exploiting the spatial overlap between high- and low-power multicolour beams. New perspectives also include the improved spatial quality control of multimode laser sources and the possibility of ultrafast routing and switching between different channels in the telecommunications domain.

In this work, we elevate the field of light manipulation in MMFs to a new dimension, involving the nonlinear interaction among multiple laser beams of different carrier wavelengths. We experimentally demonstrate that the evolution of a weak speckled beam in the visible range can be controlled using a combination of XPM and non-degenerate OIMC with an intense pump beam in the near infra-red, which undergoes its own spatial reshaping through the Kerr BSC process, but also its own spectral broadening by means of the Raman scattering process and soliton generation dynamics for very high peak powers. In our experiment, the FF infra-red beam at 1030 nm is provided by a Yb laser, while the visible beam is obtained via a nonlinear conversion from FF to SH (515 nm). Both beams are simultaneously injected into a GRIN MMF. By varying the power and modal distribution of the FF beam, the M^2 quality factor of the visible SH beam at the MMF output can be either decreased (beam cross-cleaning, BXC) or increased (beam cross-spoiling, BXS). The associated modification of the mode power distribution of the SH beam results from phase-matched IM-FWM-induced energy exchanges between its guided modes, driven by the intense FF beam. This mechanism for controlling the power exchange between modes can be compared, by analogy, to an intra-fibre controllable active spatial diffuser, sending energy from mode to mode on demand. In a first series of experiments using short laser pulses, the effect is limited by dispersive temporal walk-off. In a second set of experiments, employing long laser pulses instead, we show that beam cross-interactions can significantly alter the beam shape of the Raman cascade of Stokes lines. In this case, our experiments reveal that it is possible to reshape the number and modal content of the Stokes lines generated by a visible light beam by controlling the spatial profile and power of the near-infra-red beam. We corroborate our observations through numerical simulations. Additional elements can be found in the supplementary material. Nonlinear

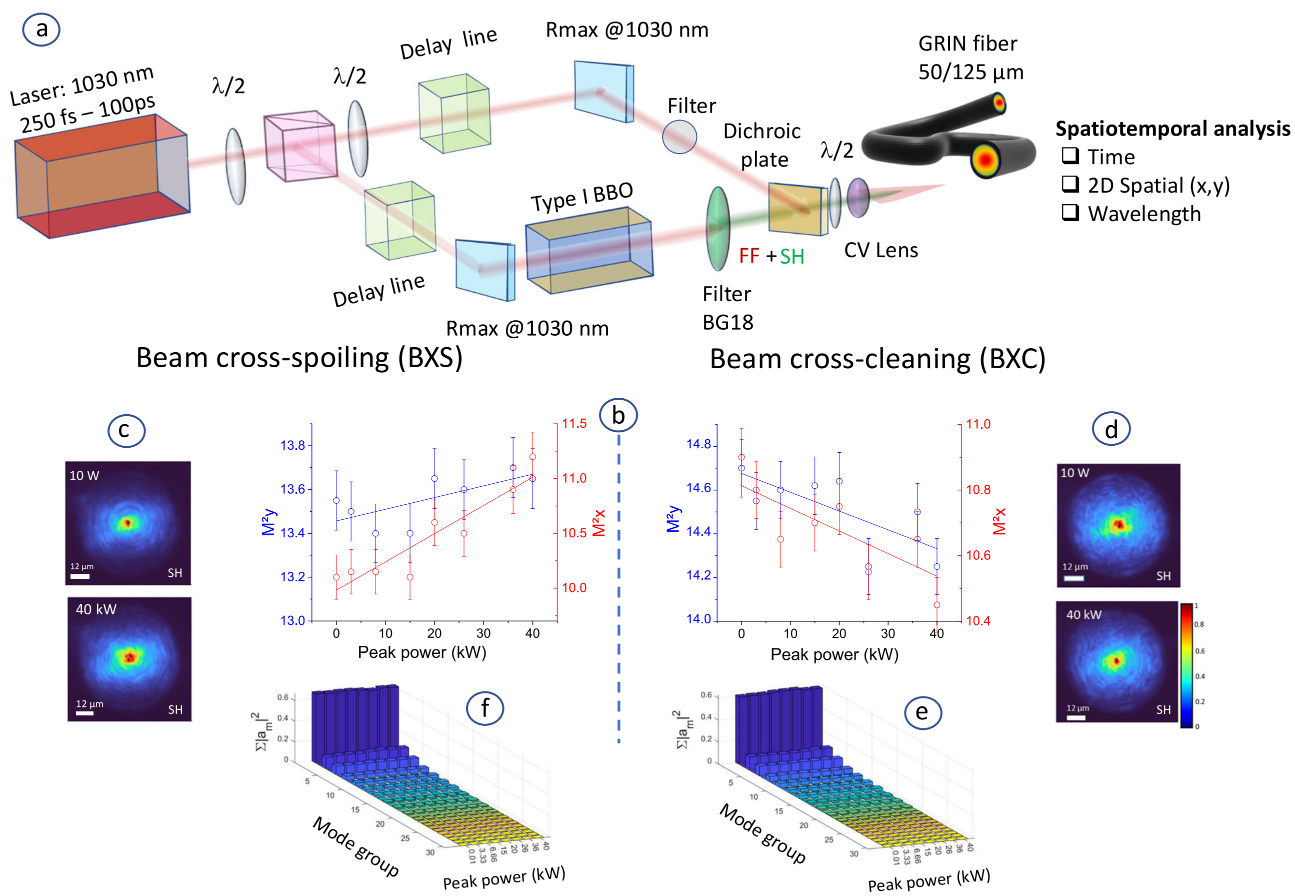

Fig. 1 | The experimental setup for light-by-light moulding in GRIN MMF and the experimental observation of beam cross-spoiling (BXS) and beam cross-cleaning (BXC). **a** A laser source with tunable pulse duration emits a beam at 1030 nm. This beam is split into two directions, one of which passes through a BBO crystal with weak conversion to SH. The two beams, referred to as FF and SH, are then combined and launched along the same GRIN MM. **b** M^2 evolution of the SH beam vs. input infra-red pump power for two different cases leading to either (left panel) BXS or (right panel) BXC; **c**, **d** examples of output near-field for the **c** BXS or **d** BXC process for low and high infra-red pump power, respectively; **e** energy per mode group for BXC; **f** energy per mode group for BXS.

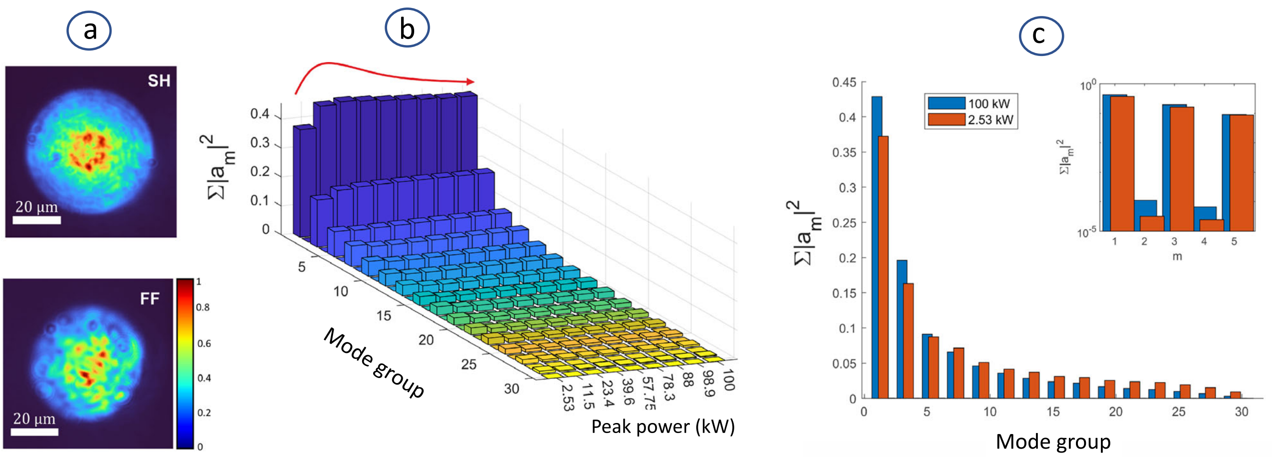

Fig. 2 | Sample cases of output beam profiles with short laser pulses and corresponding modal distributions at different power levels were numerically estimated from the beam images. a Output near-field transverse intensity profile of FF pump and SH beams; **b** energy distribution in different mode groups of the SH weak beam vs. input peak power of the infra-red pump FF, while keeping their input fibre coupling unchanged; **c** SH beam mode energy distribution at fibre output, with either 2.53 kW (orange bars) or 100 kW (blue bars) peak power pulses in FF beam; inset shows that odd mode groups remain weakly populated at all FF powers because of the coupling conditions of the FF beam straight on the fibre axis.

shaping of the spatial profile of a laser beam using another laser beam paves the way for applications such as beam switching or manipulation in ultrafast regimes, e.g., for deep biological imaging.

Results

Experimental results

In our experiments (Fig. 1a), a Gaussian beam composed of 100 ps chirped pulses at 1030 nm is first split into its two orthogonal polarisation components with adjustable powers (Fig. 1a). The vertical component of the fundamental frequency (FF) pump beam is converted to its second harmonic (SH) by a type I BBO crystal positioned for strong phase mismatch conditions; the unconverted portion of the FF is filtered out. Next, the SH is temporally and spatially superimposed with the horizontal component of the FF beam by a beam splitter and a half-waveplate, before being coupled into the 50/125 μm GRIN fibre (see Supplementary Section 7). Under these conditions, both beams retain horizontal linear polarisation, and their coupling efficiencies into the fibre can be adjusted. The green beam at 515 nm is weak enough so that its own propagation in the fibre is purely linear. On the other hand, the pump beam may undergo spatial BSC thanks to its high peak power (see Supplementary Section 2). As a result, the transverse intensity profile of the pump beam at the fibre output evolves into a clean bell shape, which is observable in both near and far fields. By adjusting the delay line between the visible SH weak beam and the strong FF pump so that the corresponding pulses no longer overlap in time, we verified that the weak SH beam remained unchanged, even in the presence of the FF beam. Conversely, when pulse synchronisation among FF and SH pulses is well-tuned, we observed significant changes in the spatial distribution of the SH at 515 nm. These could be controlled by varying the power of the FF pump beam at 1030 nm, or its spatial coupling conditions. To further investigate this process, we analysed the near (Fig. 1c, d) and far fields of the weak SH beam and performed numerical processing of both fields. This allowed the calculation of the beams' spatial phase and M^2 coefficients, helping to identify their modal energy distribution (Fig. 1b, e, f, respectively).

For the first setting of the input coupling conditions of the FF beam into the fibre (i.e., straight on axis), we observed that increasing the FF power led to mode power redistribution for the SH, whereby lower-order modes (LOMs) of the SH are favoured with respect to higher-order modes (HOMs). This spatial beam reshaping, or BXC, is obtained by the OIMC process, which does not lead to energy exchange between the FF and the SH beams. Our analysis of near and far-field images at the fibre output confirms the beam cross-shaping. The M^2 coefficient of the SH beam, calculated by standard definitions[41], followed the same trend, decreasing along both the X and Y directions as the FF power grew larger (Fig. 1b, right). The maximum FF peak power in our experiment was approximately 40 kW, limited by input face fibre degradation. This power value remains far below levels typically associated with self-focusing effects.

We could reverse the beam interaction dynamics by slightly adjusting the FF beam's input conditions (i.e., its focus point). Increasing the FF peak power led to a mode power redistribution for the SH, favouring HOMs. This BXS of the SH beam was accompanied by a corresponding increase in its M^2 coefficient (Fig. 1b, left). Near and far-field analyses confirmed this opposite trend. As we shall see in the subsequent theory section, the redistribution of energy between LOMs and HOMs of the SH beam is driven by the mode power distribution of the pump beam. That is, the FF beam modifies via OIMC the mode content of the weak SH beam. This may change the direction of energy flow among the modes of the SH beam, as testified by the corresponding decrease or increase of its quality factor. The occurrence of BXC or BXS in the SH beam is governed by nonlinear phase shifts, which either preserve or break phase-matching in the OIMC process, respectively.

In a second series of experiments (Fig. 2), we excited additional modes in the FF to achieve a better spatial overlap with the SH. In this scenario, BSC efficiency for the FF beam was reduced; a bell-shaped beam is no longer formed at the fibre output (Fig. 2a). Nevertheless, by increasing the FF power, we observed a gradual increase in the fundamental mode population of the SH beam (see Fig. 2b, c). Maximum SH BXC was observed for input FF peak powers close to 23 kW, leading to a corresponding reduction of the M^2 coefficient for the SH beam. However, the process reversed at higher input FF powers (up to 100 kW), even without altering the input coupling conditions. Namely, the proportion of energy in the fundamental and other LOMs of the SH beam now decreases as the FF power grows larger (Fig. 2b). In this regime, HOMs of the SH beam get progressively more populated, which can be interpreted as BXS, leading to an increased SH beam divergence at the fibre output. It is important to note that, to increase the peak power up to 100 kW, it was necessary to reduce the pulse duration from 100 ps down to 10 ps in order to avoid fibre damage.

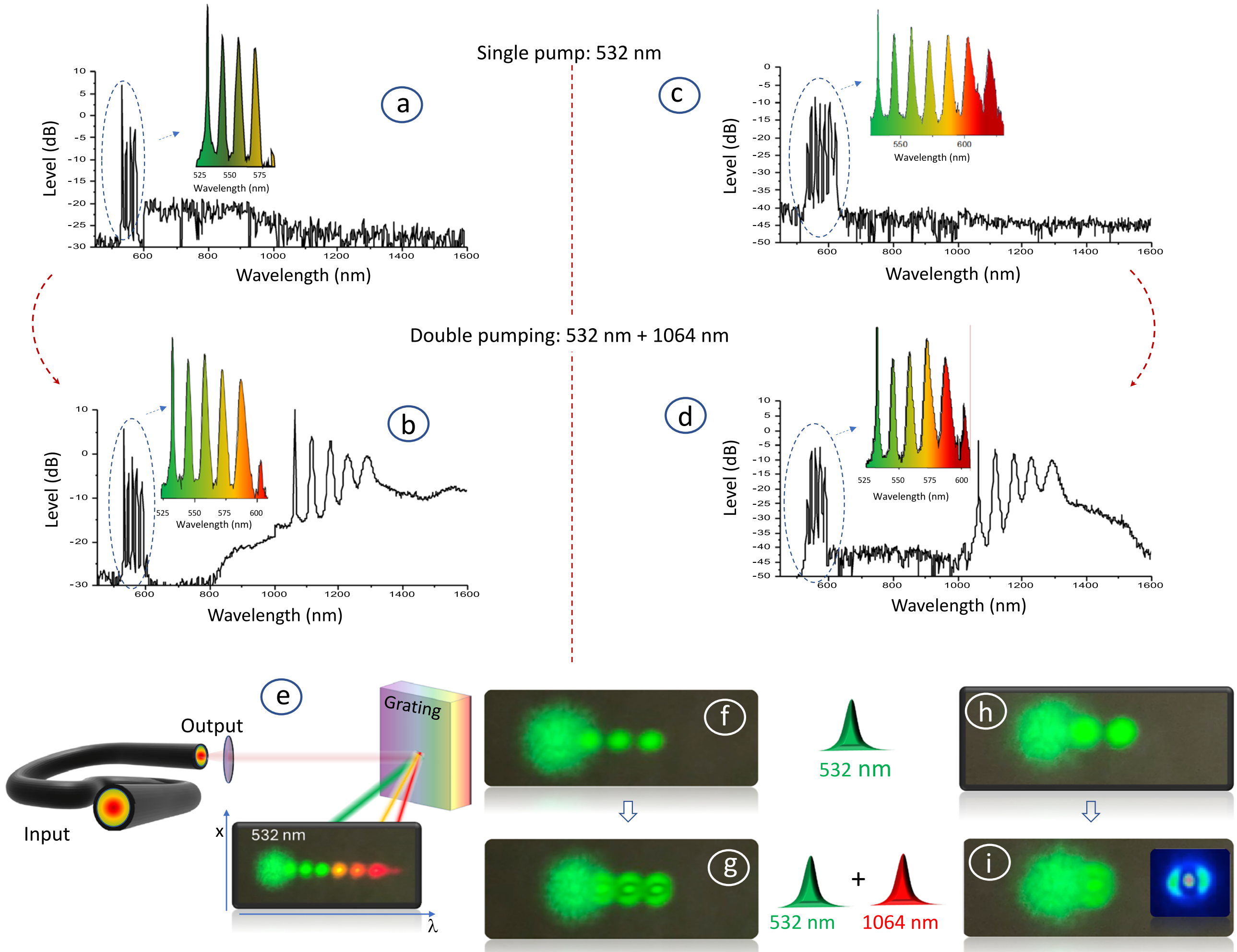

Fig. 3 | Experimental results with long laser pulses at 650 nm and beam powers large enough at FF and SH that multiple Raman Stokes sidebands can be clearly detected. At the SH, Raman Stokes sidebands are discernible at visible wavelengths. A grating is utilised to angularly separate the spectral components in the horizontal plane, thereby revealing in part their modal content along the vertical coordinate. The cross-action between the FF and the SH beam is, in this case, explored in a highly nonlinear regime. The GRIN fibre length is of 50 m, core diameter of 27 μm, peak power imbalance between infra-red FF (3 kW) and SH beams (250 W), ratio 12:1. SH Raman cascade without (**a**) or with (**b**) FF beam, demonstrating BXC-assisted enhancement of Stokes wave generation; SH Raman cascade without (**c**) or with (**d**) FF beam, demonstrating BXS-assisted suppression of Stokes wave generation; **e** experimental setup used to simultaneously observe the output beam in wavelength and spatial dimensions. Example of modal switching of the SH: beam profile without and with FF beam, panels (**f**) and (**g**), respectively. Example of modal switching and BXS of the SH beam without and with the FF beam (**h**), (**i**), respectively.

This was achieved using the same initial 250 fs Fourier transform-limited pump beam (see Methods) and changing the stretching from 100 ps to 10 ps.

As we have seen, the BXC efficiency can be limited either by the input FF peak power or by the temporal walk-off between FF and SH pulses. To further investigate the impact of BXC on multimode propagation, we conducted a third series of experiments where both individual SH and FF beams propagate in the fully nonlinear regime. We used a longer GRIN fibre (50 m) with a smaller core diameter (27 μm) (see also Supplementary Section 7); to minimise walk-off between the FF and the SH, we used another laser source that emits longer pulses, with a duration of 650 ps. By increasing the power of both SH and FF beams, while maintaining a peak power imbalance of 12:1 in favour of the infra-red pump, we observed stimulated Raman scattering (SRS) cascades at both wavelengths, involving the generation of multiple Stokes lines (see Fig. 3). The FF beam broadened spectrally beyond 1.3 μm, owing to Raman-shifted temporal soliton dynamics. On the other hand, SH propagation only produced Raman Stokes lines because of the normal dispersion regime at the SH. Furthermore, both beams undergo nonlinear propagation leading to a spatial self-cleaning process and Raman beam clean-up, as already reported in the literature[17–19]. However, in the following paragraph, we present the impact of the cross-action between the two beams (FF + SH) on the SH beam, demonstrating BXC and BXS effects within the SH Raman cascade.

Nondegenerate OIMC between FF and SH beams established a direct link between the visible and fundamental Raman cascades. This interaction allowed the visible Raman cascade to be either enhanced by the BXC (Fig. 3a, b) or suppressed (Fig. 3c, d) by the BXS effects, induced by the FF pump beam before its spectral broadening. Mutual beam interaction dynamics depend on the intensity, polarisation, and input coupling conditions of the infra-red FF beam. The observed nonlinear beam dynamics in the presence of the Kerr effect and SRS resembles the behaviour observed in the pure Kerr case. Now, BXC redistributes the energy among the transverse modes of the SH beam, which controls its Raman gain and the associated Stokes cascade. This allowed us to determine the mode content of the beam by separating its spectral components by means of a grating, as depicted in Fig. 3e.

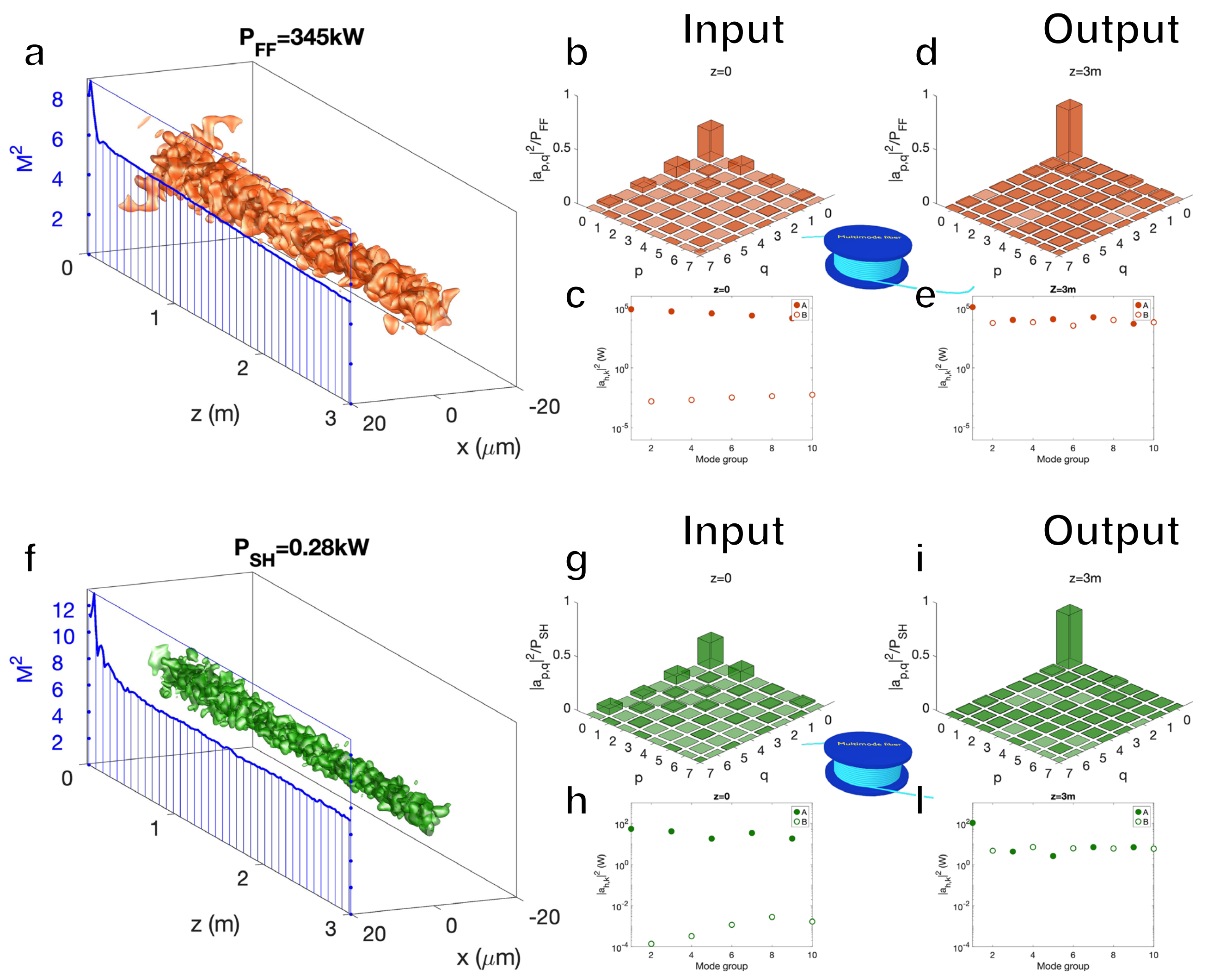

Fig. 4 | Numerically calculated beam propagation for the FF and SH beams for the case of BXC. The simulation is restricted to a 3-m long GRIN fibre as in experiments the interaction is limited by the temporal walk-off effect; **a**, **f** iso-intensity surface at the local maximum's half along the propagation coordinate z for the FF and SH beam with the calculated M^2 coefficient; **b**, **d**, **g**, **i** modal decomposition at input and output of FF (SH) beams respectively; **c**, **e**, **h**, **l** detail on modal decomposition for FF (SH) illustrating the difference in power distribution between odd- (**a**) and even- (**b**) order mode groups at the fibre input and output respectively (group 1 contains the fundamental mode).

Interestingly, we observed that the oscillating transverse mode of the Raman cascade could change (Fig. 3f, g) and that the number of Stokes lines could be decreased with a change in the transverse mode (Fig. 3h, i). This light-by-light switching was observed across varying numbers of Stokes lines, demonstrating that spatial reshaping of the SH beam preceded the generation of its own Stokes lines. We also note that the modal cascade with the appearance of the LP_{02}-like mode remains stable over all three Stokes lines, apparently blocking or stabilising the Raman beam clean-up process (Fig. 3f, g). We also measured that more than 80% of the energy contained in the three Stokes Raman lines oscillating in the fundamental mode is transferred into the LP_{02}-like mode, clearly illustrating the highly energetic impact that this cross-process can introduce.

Numerical results

We conducted numerical simulations to analyse the spatial reshaping of the weak SH beam under BXC or BXS, influenced by the FF beam. We used two coupled equations, one for the FF and one for the SH beam, which interact via asymmetric OIMC and XPM, owing to their different wavelengths, powers, and temporal walk-off between their pulses (see Methods). We also included the linear random mode coupling terms. In the linear propagation regime, no evolution of the beams was observed; all excited modes retain their energy, and the M^2 coefficient remains constant for both beams (see Supplementary Section 3a). Simulations show the presence of a spatial BSC process (Fig. 4) in the pump beam whenever its power grows above a certain threshold value. As a result, the weak SH beam undergoes BXC, with spatial remodelling leading to power transfer into its fundamental mode at the expense of HOMs (Fig. 4f). This BXC occurs without any energy exchange between the two beams: no second-order nonlinearity is included in the model. Moreover, when the input peak power of the FF beam is further increased, we observed that BXC starts to saturate, until it gradually reverses (Fig. 5). In this regime, the LOMs of the SH beam are now depleted in favour of its HOMs (Fig. 5f). This inversion of behaviour occurs without any modification of the spatial input coupling conditions of the FF or the SH beams, at variance with the experimental results that we illustrated in Fig. 2. Here, the only parameter that varied in our simulations was the FF input peak power. It is important to note that the brightness improvement of the FF pump beam associated with BSC remains limited when compared with the brightness improvement of the weak SH beam under BXC.

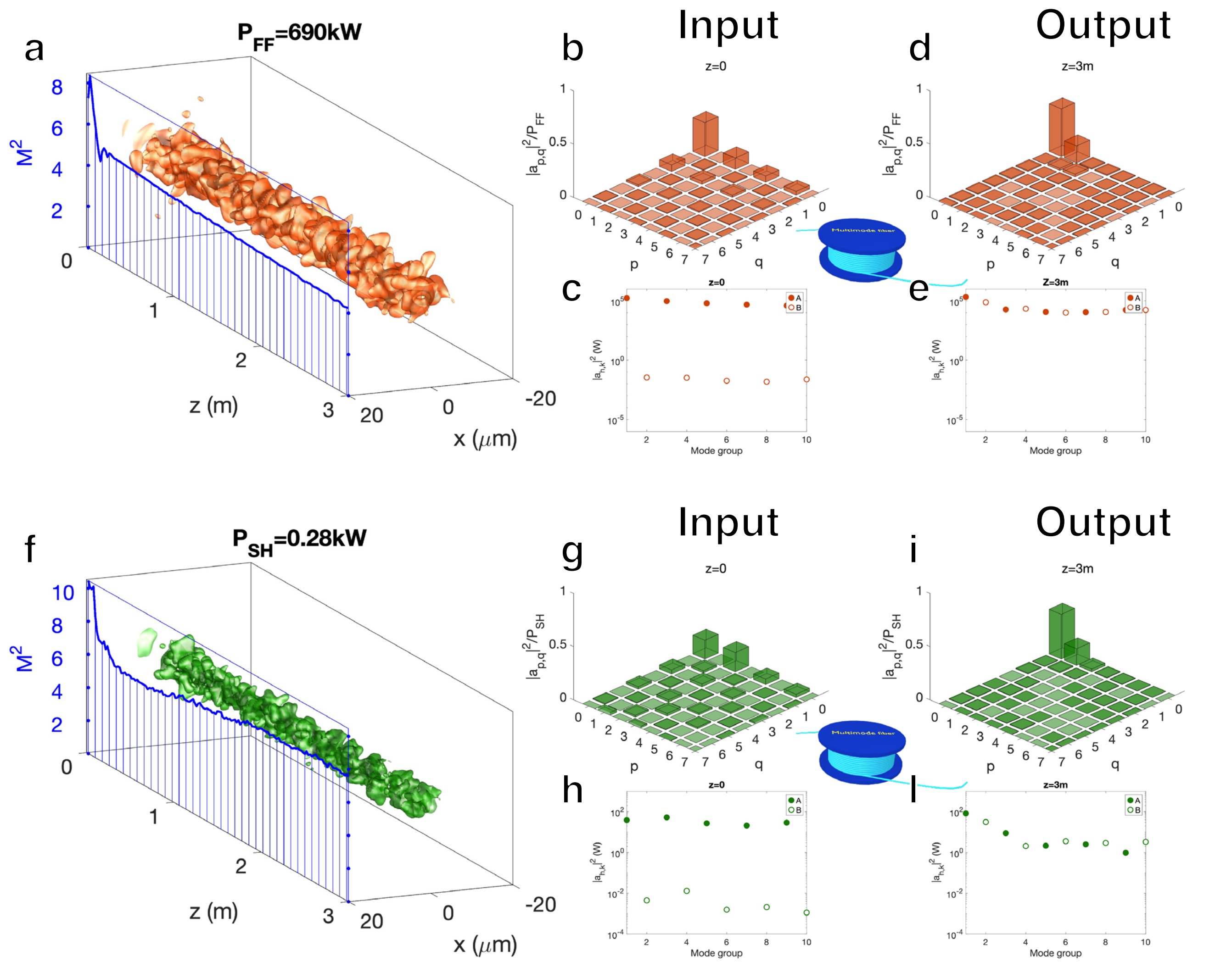

Fig. 5 | Numerically calculated beam propagation for the FF and SH beams for the case of BXS. The simulation is restricted to a 3-m long GRIN fibre as in experiments the interaction is limited by the temporal walk-off effect; **a**, **f** iso-intensity surface at the local maximum's half along the propagation coordinate z for the FF and SH beam with the calculated M^2 coefficient; **b**, **d**, **g**, **i** modal decomposition at input and output for FF (SH) beams, respectively; **c**, **e**, **h**, **l** detail on modal decomposition for FF (SH) illustrating the difference in power distribution between odd- (**a**) and even- (**b**) order mode groups at the fibre input and output respectively (group 1 contains the fundamental mode).

We considered input Gaussian beams for both the FF and the SH, centred on the fibre axis in simulations. As a result, only even modes are excited (Fig. 4c, h and Fig. 5c, h). In the occurrence of both BXC and BXS of the weak SH beam, we observed that odd modes remain largely unpopulated; this phenomenon has also been highlighted in the simpler case of BSC, as noted in ref. 42. The authors identified that mode groups containing radially symmetric modes are more populated than odd modes, a natural consequence of injecting a radially symmetric coherent beam into the MMF. They also noted that nonlinear modal interactions have varying efficiencies due to the significant differences in nonlinear overlap coefficients between modes, which significantly affect the rate of convergence toward a steady-state mode power distribution.

Temporal walk-off between the weak SH and the infra-red FF beam plays a significant role in the mechanism of BXC or BXS. To evaluate this, we ran numerical simulations without temporal walk-off (see Supplementary Section 3b). The results revealed a significant increase in modulation from the infra-red to the green beam, along with a more pronounced change in the M^2 coefficient. Experimentally, temporal walk-off can be minimised by using two closely spaced wavelengths, or a longer pulse relative to the propagation time in the fibre, as realised in our third experiment in a strong nonlinear propagation regime involving a remodelling of the Raman cascade.

Discussion

In this work, we introduce and experimentally demonstrate the intriguing possibility of controlling the brightness of a weak beam via its interaction with an intense light beam at a different frequency, mediated by OIMC and XPM. This method adds an additional degree of freedom in the spatial BSC process that has been observed so far in multimode fibres. The cross-beam interaction can be regarded as an extension of the BSC mechanism, in which the self-phase modulation driving the cleaning process is replaced by a nonlinear phase shift (or cross-phase modulation) induced through interaction with an additional beam. In other words, the longitudinal grating formed in the BSC regime, arising from the combined action of the Kerr effect and the self-imaging process in the parabolic fibre, can strongly impact other beams, whether weak or strong, that propagate simultaneously within the fibre. This constitutes a new nonlinear propagation regime that is more versatile and readily controllable.

Cross-beam interaction is a purely conservative process, occurring without mutual amplification or absorption. It significantly expands the domain of application of beam cleaning processed in Kerr media by enhancing the nonlinear interactions between copropagating waves. The modal overlap between wavelengths, which depends on the transverse position in the fibre core (see Fig. 1), enables control over the modal content of the weak SH beam. This is achieved via the spatiotemporal distribution of the pump intensity, which induces XPM-induced phase-matching for the spatial OIMC processes for the weak SH beam. The influence of XPM within a parametric FWM system is well established, and it was earlier demonstrated in microstructure fibres[43] (see Supplementary Section 1).

Consequently, the power of the FF beam can control the rate and direction of energy transfer between modes in the weak SH. Under the combined self-imaging and Kerr effects, beam propagation in a GRIN optical fibre is longitudinally modulated by a transient index grating, which facilitates phase-matching of degenerate spatial IM-FWM processes, provided the peak power is sufficient. This phase-matching, induced by longitudinal intensity modulation, can also occur between waves at different frequencies, leading to geometric parametric instabilities[15], or between spatial modes, leading to the spatial BSC[16]. By coupling a high-power pump beam with a weak signal beam, one may control the efficiency of nondegenerate OIMC within each beam and change the direction of the energy flow among its modes, leading to either improvement or degradation of a laser beam quality. It should also be emphasised that the FF beam disturbs the SH beam by increasing or decreasing the energy transfer dynamics between its modes, similar to the effect of a local diffuser placed within the fibre core. This spatial energy redistribution in the SH beam can be associated with the transient evolution of its out-of-equilibrium entropy as a function of the FF peak power (see Supplementary Section 4)[40]. Numerical simulations show that the higher the slope of the entropy of the SH, the more effective the energy dispersion on the other transverse modes is, which increases the M^2 coefficient and decreases the beam quality. By pushing cross-cleaning to its limit, we numerically predict a strong transfer (52%) of energy from a weak speckle beam to a single transverse mode using a high-power FF speckle beam (see Supplementary Section 5)

As a dramatic manifestation of the possible consequences of XPM-based control of different laser beams in MMFs, we experimentally demonstrated the ability to enhance or suppress the Raman cascade of visible radiation generated by SH of another infrared beam, based on the mere control of its input coupling condition into the fibre. We envisage that these findings will have many far-reaching impacts on applying nonlinear multimode fibres for high-power laser beam technologies.

Beyond this demonstration of the cross-action between two beams propagating simultaneously in a multimode fibre, we would also like to highlight that these multi-wave nonlinear interaction processes may find numerous potential applications. Let us mention, for instance, multiplexed coherent anti-Stokes Raman spectroscopy and nonlinear fluorescence spectroscopy in multimode fibres, where multiple wavelengths propagate simultaneously, enabling high-resolution transverse imaging of biological samples over a wide spectral range[33,44]. Another example involves the process of second-harmonic generation in multimode fibres, which gives rise to single-mode emission owing to the cross-action between the fundamental pump and its harmonic[45].

Methods

Experiments

The detailed experimental setup is presented in Fig. 1a. It consists of a femtosecond–picosecond laser source delivering pulses between 250 fs and 100 ps (1030 nm), and a laser source with a pulse duration of 650 ps. The initial beam is separated into two parts using a polariser and a half-wave plate. The first beam is converted into a BBO crystal cut for SH generation, and the remaining part of the infrared pump is removed using a BG18 filter. Thus, the SH is not generated inside the optical fibre, but it is coupled into it after conversion in a BBO crystal. The second part of the pump beam is attenuated by a passive filter and resynchronised with the SH of the first beam by means of two delay lines placed on each arm of the Mach-Zehnder interferometer. The synchronisation accuracy is estimated to be 0.2 ps based on the optimisation of the third harmonic generation correlation between SH and FF beams. A wideband dichroic plate is used. The two beams are temporally and spatially superimposed at the fibre input with linear polarisation states by using a half-wave plate at the FF wavelength placed before the coupling lens. The fibre excitation process is carried out using a converging lens with a focal length of 50 mm. The output beams are analysed by two CCD cameras, allowing near- and far-field recordings for both beams. The first fibre is a 10 m long GRIN 50/125 μm multimode guide. A second GRIN fibre, 50 m long with a 27 μm core diameter, is instead used for Raman cascade generation. The images in Fig. 3f–i are obtained by spatio-spectral analysis, using an optical grating to disperse the light in the horizontal dimension and reveal the far-field image of the beam in the vertical plane (Fig. 3e). The results presented in Figs. 2 and 3 are obtained by observing the green beam in the near-field domain and by readjusting only the coupling of the FF beam. The far-field associated with the green beam is then obtained in a second step, when collecting the final results.

Numerical simulations

For the spatial propagation in both the FF beam and SH, we solved the GNLSE by considering an input Gaussian beam with a FWHM of 35 μm for both the SH and the FF. These simulations consider diffraction, material dispersion, waveguide contribution and Kerr effect ($n_2 = 2.6 \times 10^{-20}$ m^2/W). The scalar propagation for both field is solved via a split-step algorithm in the domain of spatial frequencies with a 2D fast Fourier transform for the diffraction term and in the spatial domain for the waveguide contribution and Kerr effect. The two equations are incoherently coupled via the term of cross-phase modulation as follows:

$$\begin{cases} \frac{\partial A_{FF}}{\partial z} = i\frac{\nabla_\perp^2 A_{FF}}{2k_{FF}} + i\frac{\left(k^2(x,y)-k_{FF}^2\right)}{2k_{FF}}A_{FF} + i\gamma_{FF}\left(|A_{FF}|^2 + 2|A_{SH}|^2\right)A_{FF}, \\ \frac{\partial A_{SH}}{\partial z} = i\frac{\nabla_\perp^2 A_{SH}}{2k_{SH}} + i\frac{\left(k^2(x,y)-k_{SH}^2\right)}{2k_{SH}}A_{SH} + i\gamma_{SH}\left(|A_{SH}|^2 + 2|A_{FF}|^2\right)A_{SH} \end{cases} \tag{1}$$

In equation 1 A_{SH} and A_{FF} denote the complex field evelopes at SH and FF respectively and $\gamma_i = n_2\omega_i/c$ denote the nonlinear coefficients at the two carrier wavelengths. The first term in the right-hand side of the equation denotes the diffraction of the beam, the second one the waveguide condition and the third term accounts for the non-linear effects. Temporal effects are not included (to reduce the computational effort), and the consequences of the temporal walk-off effect are implemented by limiting the propagation length where the XPM interaction is active. In the simulations after 3 m the cross terms between SH and FF were eliminated. It is also worth noting that in the FF equation, the cross-phase modulation term proportional to $|A_{SH}|^2$, could be omitted as the $I_{FF} \gg I_{SH}$. While the power of the SH was kept constant at $P_{SH} = 0.28$ kW, and the FF was increased until $P_{FF} = 600$ kW. The waveguide specifications were for a GRIN fibre 50/125. We assumed core and cladding refractive indices at FF of 1.4653 and 1.45, respectively. At SH, the refractive indices are 1.4765 and 1.4615. The numerical simulation was performed with a longitudinal step of 2 μm, a transverse spatial domain of 90 μm × 90 μm with a resolution of 0.35 μm. The random mode coupling was simulated by weak random deformations of the refractive index with a coarse step applied at a random distance of an average length of 5 mm.

The modal decomposition performed both in the experimental and the simulations was done by means of a stochastic parallel gradient descent optimisation algorithm[46]. The optimisation was supervised by epochs of 100 times the number of modes considered, stopping criteria was either 100 epochs or an increase in the correlation experimental–simulation lower than 10^{-4}. For the mode decomposition of the simulated data, the far-field requirement was omitted as the phase of the beam was known.

Data availability

Data underlying the results presented in this paper are not publicly available at this time but may be obtained from the corresponding author upon request.

Code availability

Codes used in this paper are not publicly available at this time but may be obtained from the corresponding author upon request.

References

1. Islam, M. N., Mollenauer, L. F., Stolen, R. H., Simson, J. R. & Shang, H. T. Cross-phase modulation in optical fibers. *Opt. Lett.* **12**, 625–627 (1987).
2. Alfano, R. R., Baldeck, P. L. & Ho, P. P. Cross-phase modulation and induced focusing due to optical nonlinearities in optical fibers and bulk materials. *J. Opt. Soc. Am. B* **6**, 824–829 (1989).
3. Manassah, J. T. Focusing effects of IPM on a probe pulse propagating in a χ(3) medium. *Opt. Lett.* **14**, 396–398 (1989).
4. Stentz, A. J., Kauranen, M., Maki, J. J., Agrawal, G. P., & Boyd, R. W Induced focusing and spatial wave breaking from cross-phase modulation in a self-defocusing medium. *Opt. Lett.* **17**, 19–21 (1992).
5. Lopez Lago, E. & de la Fuente, R. Copropagation of two waves of different frequencies and arbitrary initial polarization states in an isotropic Kerr medium. *Phys. Rev. A* **60**, 549–558 (1999).
6. Agrawal, G. P. Induced focusing of optical beams in self-defocusing nonlinear media. *Phys. Rev. Lett.* **64**, 2487–2490 (1990).
7. Hickmann, J. M., Gomes, A. S. L. & de Araujo, C. B. Observation of spatial cross-phase modulation effects in a self-defocusing nonlinear medium. *Phys. Rev. Lett.* **68**, 3547–3550 (1992).
8. Schnack, M., Hellwig, T., Brinkmann, M. & Fallnich, C. Ultrafast two-color all-optical transverse mode conversion in a graded-index fiber. *Opt. Lett.* **40**, 4675–4678 (2015).
9. McGuinness, H. J., Raymer, M. G., McKinstrie, C. J. & Radic, S. Quantum frequency translation of single-photon states in a photonic crystal fiber. *Phys. Rev. Lett.* **105**, 093604 (2010).
10. Krupa, K. et al. Bragg-Scattering conversion at telecom wavelengths towards the photon counting regime. *Opt. Express* **20**, 27220–27225 (2012).
11. Hellwig, T., Walbaum, T. & Fallnich, C. Optically induced mode conversion in graded-index fibers using ultra-short laser pulses. *Appl. Phys. B* **112**, 499–505 (2013).
12. Lacava, C. et al. Intermodal Bragg-scattering four wave mixing in silicon waveguides. *J. Lightwave Technol.* **37**, 1680–1685 (2019).
13. Wright, L. G., Christodoulides, D. N. & Wise, F. W. Controllable spatiotemporal nonlinear effects in multimode fibres. *Nat. Photonics* **9**, 306–310 (2015).
14. Tzang, O., Caravaca-Aguirre, A. M., Wagner, K. & Piestun, R. Adaptive wavefront shaping for controlling nonlinear multimode interactions in optical fibres. *Nat. Photonics* **12**, 368–374 (2018).
15. Krupa, A. et al. Observation of geometric parametric instability induced by the periodic spatial self-imaging of multimode waves. *Phys. Rev. Lett.* **116**, 183901 (2016).
16. Krupa, K. et al. Spatial beam self-cleaning in multimode fibres. *Nat. Photonics* **11**, 234–241 (2017).
17. Liu, Z., Wright, L. G., Christodoulides, D. N. & Wise, F. W. Kerr self-cleaning of femtosecond-pulsed beams in graded-index multimode fiber. *Opt. Lett.* **41**, 3675–3678 (2016).
18. Krupa, K. et al. Multimode nonlinear fiber optics, a spatiotemporal avenue. *APL Photonics* **4**, 110901 (2019).
19. Mohammadzahery, Z., Jandaghi, M., Aghayari, E. & Nabavi, H. Observation of spatial nonlinear self-cleaning in a few-mode step-index fibre for special distributions of initial excited modes. *Sci. Rep.* **11**, 24350 (2021).
20. Deliancourt, E. et al. Kerr beam self-cleaning on the LP11 mode in graded-index multimode fibers. *OSA Contin.* **2**, 1089–1096 (2019).
21. Wu, Y., Pourbeyram, H., Christodoulides, D. N. & Wise, F. W. Weak beam self-cleaning of femtosecond pulses in the anomalous dispersion regime. *Opt. Lett.* **46**, 3312–3315 (2021).
22. Deliancourt, E. et al. Wavefront shaping for optimized many-mode Kerr beam self-cleaning in graded-index multimode fiber. *Opt. Express* **27**, 17311–17321 (2019).
23. Leventoux, Y. et al. 3D time-domain beam mapping for studying nonlinear dynamics in multimode optical fibers. *Opt. Lett.* **46**, 66–69 (2021).
24. Guenard, R. et al. Kerr self-cleaning of pulsed beam in an ytterbium doped multimode fiber. *Opt. Express* **25**, 4783–4792 (2017).
25. Guenard, R. et al. Nonlinear beam self-cleaning in a coupled cavity composite laser based on multimode fiber. *Opt. Express* **25**, 22219–22227 (2017).
26. Wright, L. G., Christodoulides, D. N. & Wise, F. W. Spatiotemporal mode-locking in multimode fibre lasers. *Science* **358**, 94–97 (2017).
27. Niang, A. et al. Spatial beam self-cleaning and supercontinuum generation with Yb-doped multimode graded-index fiber taper based on accelerating self-imaging and dissipative landscape. *Opt. Express* **27**, 24018–24028 (2019).
28. Eftekhar, M. A. et al. Accelerated nonlinear interactions in graded-index multimode fibres. *Nat. Commun.* **10**, 1638 (2019).
29. Teğin, U., Rahmani, B., Kakkava, E., Psaltis, D. & Moser, C. Single-mode output by controlling the spatiotemporal nonlinearities in mode-locked femtosecond multimode fiber lasers. *Adv. Photonics* **2**, 056005–056005 (2020).
30. Wright, L. G. et al. Mechanisms of spatiotemporal mode-locking. *Nat. Phys.* **16**, 565–570 (2020).
31. Wu, Y., Christodoulides, D. N. & Wise, F. W. Multimode nonlinear dynamics in spatiotemporal mode-locked anomalous-dispersion lasers. *Opt. Lett.* **47**, 4439–4442 (2022).
32. Fabert, M. et al. Coherent combining of self-cleaned multimode beams. *Sci. Rep.* **10**, 20481 (2021).
33. Moussa, N. O. et al. Spatiotemporal beam self-cleaning for high-resolution nonlinear fluorescence imaging with multimode fibre. *Sci. Rep.* **11**, 18240 (2021).
34. Pourbeyram, H. et al. Direct observations of thermalization to a Rayleigh–Jeans distribution in multimode optical fibres. *Nat. Phys.* **18**, 685–690 (2022).
35. Baudin, K. et al. Classical Rayleigh-Jeans condensation of light waves: observation and thermodynamic characterization. *Phys. Rev. Lett.* **125**, 244101 (2020).
36. Ferraro, M., Mangini, F., Zitelli, M. & Wabnitz, S. On spatial beam self-cleaning from the perspective of optical wave thermalization in multimode graded-index fibers. *Adv. Phys.* **8**, 2228018 (2023).
37. Ferraro, M. et al. Calorimetry of photon gases in nonlinear multimode optical fibers. *Phys. Rev. X* **14**, 021020 (2024).
38. Ferraro, M. et al. Multimode optical fiber beam-by-beam cleanup. *J. Lightwave Technol.* **41**, 3164–3174 (2023).
39. Zhong, Q., Wu, F. O., Hassan, A. U., El-Ganainy, R. & Christodoulides, D. N. Universality of light thermalization in multimoded nonlinear optical systems. *Nat. Commun.* **14**, 370 (2023).
40. Ren, H. et al. Dalton's law of partial optical thermodynamic pressures in highly multimoded nonlinear photo systems. *Opt. Lett.* **49**, 1802–1805 (2024).
41. Orazio Svelto. *Principe of Lasers*. Springer, Fifth edition, p 492 (2010).
42. Baudin, K. et al. Rayleigh–Jeans thermalization vs beam cleaning in multimode optical fibers. *Opt. Commun.* **545**, 129716 (2023).

43. Fan, J. & Migdall, A. Phase-sensitive four-wave mixing and Raman suppression in a microstructure fiber with dual laser pumps. *Opt. Lett.* **31**, 18 (2006).
44. Mansuryan, T. et al. Spatial division multiplexing for multiplex coherent anti-stokes Raman scattering. *J. Lightwave Technol.* **41**, 6875–6883 (2023).
45. Ceoldo, D. et al. Second harmonic generation in multimode graded-index fibers: spatial beam cleaning and multiple harmonic side-band generation. *Opt. Lett.* **42**, 971–974 (2017).
46. Kim, B., Na, J., Kim, J., Kim, H. & Jeong, Y. oonchan Modal decomposition of fiber modes based on direct far-field measurements at two different distances with a multi-variable optimization algorithm. *Opt. Express* **29**, 21502–21520 (2021).

Acknowledgements
V.C. thanks the National Research Agency under the Investments for the Future programme with the reference ANR-10-LABX-0074-01 Sigma-LIM, the ANR-23-CE08-0021-02, ANR-21-ESRE-0007 ADD4P, ANR-24-CE46-7295-01-ACT and the EIC Pathfinder project "Multiscope" N°: 101185664. Y.A. acknowledges receiving a postdoctoral fellowship (ED481D-2024-001) from the Xunta de Galicia (Spain). K. Krupa acknowledges Narodowe Centrum Nauki (OPUS 2023/49/B/ST7/01482) and Narodowa Agencja Wymiany Akademickiej (BPN/BIT/2024/00035). This work received funding from the European Research Council (ERC) under the European Union's Horizon 2020 research and innovation programme under grant agreement No.950618 (STREAMLINE). B.W. also acknowledges the support of the Région Nouvelle Aquitaine (SPINAL Project).

Author contributions
T. M., Y. A., V. C., K. K. B. W. and W. A. G. carried out the experiments. A. T., Y. A., M. F., S. W., A. P. and F. M. realised numerical simulations and proposed theoretical interpretations. All authors analysed the obtained results, participated in the discussions and in the writing of the paper.

Competing interests
The authors declare no competing interests.

Additional information
Supplementary information The online version contains supplementary material available at https://doi.org/10.1038/s41467-026-70057-3.

Correspondence and requests for materials should be addressed to Vincent Couderc.

Peer review information *Nature Communications* thanks the anonymous, reviewer(s) for their contribution to the peer review of this work. A peer review file is available.